

Cluster Reconstruction from Combined Strong and Weak Lensing

Prasenjit Saha

Department of Physics, University of Oxford, UK

Liliya L.R. Williams

Department of Physics and Astronomy, Univ. of Victoria, BC, Canada

Hanadi M. AbdelSalam

Kapteyn Sterrewacht, Rijksuniversitaet Groningen, The Netherlands

Abstract. The lensing information provided by multiple images, arclets, and statistical distortions can all be formulated as linear constraints on the arrival-time surface, and hence on the mass distribution. This reduces cluster lens reconstruction from combined strong and weak lensing to a standard type of inversion problem. Moreover, the mass sheet degeneracy is broken if there are sources at different redshifts.

This paper presents a reconstruction technique based on these ideas, and a mass map and discussion of C11358+62.

1. Introduction

The different regimes of cluster lensing—the inner region where multiple images, including giant arcs are found, further out where highly sheared but singly imaged arclets are found, and the outer regions showing statistical shear—have in the past been approached with quite different modeling methods. But these apparently separate regimes can be studied in a unified way. The key is to express lensing information in terms of the arrival surface.

In earlier work (see AbdelSalam et al. 1998) we combined the multiple-image and arclet regimes and argued that extending to statistical shear was a straightforward algorithmic issue. This paper makes that extension.

2. The arrival-time surface

The creature we will mostly be concerned with is the scaled arrival-time surface $\tau(\boldsymbol{\theta})$, and it is expressed as follows:

$$\tau(\boldsymbol{\theta}) = \frac{1}{2}(\boldsymbol{\theta} - \boldsymbol{\beta})^2 - \frac{(D_{\text{ls}}/D_{\text{s}})}{\pi} \int \ln |\boldsymbol{\theta} - \boldsymbol{\theta}'| \kappa(\boldsymbol{\theta}') d^2\boldsymbol{\theta}' \quad (1)$$

$$= \frac{1}{2}(\boldsymbol{\theta} - \boldsymbol{\beta})^2 - 2(D_{\text{ls}}/D_{\text{s}}) \nabla^{-2} \kappa(\boldsymbol{\theta}). \quad (2)$$

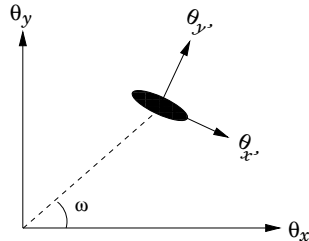


Figure 1. Schematic of an arclet elongated with position angle ω , with $(\theta_{x'}, \theta_{y'})$ being a coordinate system aligned with the elongation.

As usual, θ and β are angular locations on the image and source planes respectively, and the D 's are angular diameter distances in units of c/H_0 . However, κ is the convergence *for sources at infinity*, (hence the factors of D_{ls}/D_s) to make dealing with multiple source redshifts more convenient. The form of Eq. (1) is then familiar, while Eq. (2) is just a shorthand for the same thing with ∇^{-2} denoting an ‘inverse Laplacian operator’ in two dimensions.

To get back to physical arrival time and surface density we use

$$\text{time} = h^{-1} \tilde{z} \times 80 \text{ days arcsec}^{-2} \times \tau(\theta) \quad (3)$$

$$\text{surface density} = h^{-1} \tilde{z} \times 1.2 \times 10^{11} M_{\odot} \text{ arcsec}^{-2} \times \kappa(\theta) \quad (4)$$

where $\tilde{z} = (1 + z_1)D_1$ but is $\simeq z_1$.

Lensing data constrain the arrival-time surface and hence the mass distribution $\kappa(\theta)$ in various ways. We can identify three types of constraints: on the values of the arrival time surface at particular points, on the first derivative, and on the second derivative.

The first type is when we know the height difference between two or more points on the arrival-time surface. This is all-important in time-delay quasars and H_0 measurements, because time delays supply just this height-difference information. But it is not relevant to cluster lensing, at least not yet, though we can always hope for a supernova in a giant arc.

The second type of constraint comes from stating Fermat’s principle at each image location, i.e.,

$$\nabla \tau(\theta_{\text{image}}) = 0. \quad (5)$$

Since image positions θ_{image} can generally be measured very accurately, the Eq. (5) tells us that the arrival-time surface has zero gradient at some known point. This type of constraint is only useful if we have multiple images; in that case we have $2\langle \text{images} \rangle$ equation of the form (5) but only two unknown source coordinates to solve for, giving us some net constraints on $\kappa(\theta)$. In general there are $2(\langle \text{images} \rangle - \langle \text{sources} \rangle)$ constraints.

The third type of constraint involves the curvature or second derivative of the arrival-time surface, and may come from either arclets or from statistical distortions.

Consider first a situation like Fig. 1, where an arclet is observed elongated with position angle ω . If we are confident that the arclet has been elongated by a factor of at least k , we can consider the coordinate system $(\theta_{x'}, \theta_{y'})$ aligned

with the elongation and write

$$k \left| \frac{\partial^2}{\partial \theta_{x'}^2} \tau(\boldsymbol{\theta}_{\text{image}}) \right| \leq \left| \frac{\partial^2}{\partial \theta_{y'}^2} \tau(\boldsymbol{\theta}_{\text{image}}) \right|. \quad (6)$$

Further, since ω is known, we can transform Eq. (6) to the unrotated (θ_x, θ_y) coordinates. It is not necessary to have highly accurate values of the elongation or its orientation ω —all we have to do is set k conservatively enough that the inequality (6) is valid. The arclet used may itself be part of a multiple-image system; if so we will have to guess the parity to remove the absolute value signs in (6).

The same idea can be applied to statistical distortion. In this case the data provide an estimate and uncertainty

$$\frac{\gamma_i}{1 - \kappa} = g_i \pm \Delta g_i, \quad (7)$$

where γ_i and κ are components of the second derivative of $\tau(\boldsymbol{\theta})$. We can rewrite this in various ways, such as

$$(1 - \kappa(\boldsymbol{\theta}_{\text{image}}))g_i - \Delta g_i \leq \gamma(\boldsymbol{\theta}_{\text{image}}) \leq (1 - \kappa(\boldsymbol{\theta}_{\text{image}}))g_i + \Delta g_i. \quad (8)$$

(We have assumed $\kappa \Delta g_i$ is negligible here.)

A key feature of the constraint equations (5), (6), and (8) is that they are all linear in the unknowns $\boldsymbol{\beta}$ and $\kappa(\boldsymbol{\theta})$. Which is to say¹

$$\begin{pmatrix} \text{Lensing} \\ \text{data} \end{pmatrix} = \begin{pmatrix} \text{A} & \text{messy} & \text{but} & \text{linear} & \text{operator} \\ \text{also} & \text{involving} & \text{the} & \text{same} & \text{data} \end{pmatrix} \begin{pmatrix} \text{The} \\ \text{lens's} \\ \text{projected} \\ \text{mass} \\ \text{distribution} \end{pmatrix} \quad (9)$$

and moreover this is true for all lensing regimes: multiple-image, arclet, and statistical shear.

3. Mass reconstruction

Eq. (9) summarizes the advantage of casting the observational information as constraints on the arrival-time surface. Lens reconstruction is reduced to a linear inversion problem. It is (as symbolized by the 2×5 matrix) a highly underdetermined problem, so in order to reconstruct the lens it is necessary to add extra information (sometimes called a prior). Also as indicated in the 2×5 matrix, the data enter into the linear operator—an unusual complication. However, as we

¹With one exception: scalar magnification data are quadratic in κ and so (9) does not apply. Taylor and collaborators (see e.g., Dye & Taylor 1998) have developed reconstruction techniques for this case. However, if magnification information is present along with shear information, together they give (at least in principle) the tensor magnification which is linear in κ , and so (9) again applies.

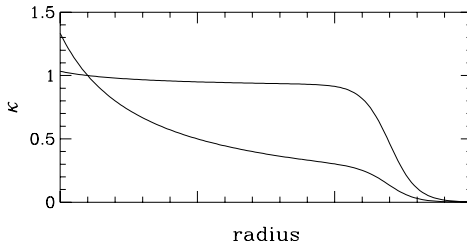


Figure 2. At fixed redshift, the mass sheet degeneracy leaves $1 - \kappa$ uncertain by a multiplicative factor, while the monopole part of κ is undetermined outside the region of the images. As a result, the two mass profiles shown will produce identical multiple-image and shear data out to the cliff.

discussed above, the data enter there either as image positions which are known very accurately, or as inequalities which can be set conservatively; so this issue does not introduce new difficulties.

At least four different possibilities for lens reconstruction now suggest themselves

- Put $\tau(\boldsymbol{\theta})$ on a grid and regularize. This may be the simplest approach.
- Use basis function expansions for $\kappa(\boldsymbol{\theta})$ and $\tau(\boldsymbol{\theta})$. A Fourier-Bessel expansion

$$\tau(\boldsymbol{\theta}) = \sum_{mn} c_{mn} J_m(k_{mn}\theta) \exp(im\phi)$$

is particularly attractive as it would trivially relate τ and κ .

- Pixellate $\kappa(\boldsymbol{\theta})$ and regularize. This is the one we have implemented. The mass is distributed on square tiles, each having constant but adjustable density, and $\tau(\boldsymbol{\theta})$ comes from computing Eq. (1) exactly. Note that although the mass distribution is discontinuous, the arrival-time surface is smooth. Unlike in the two previous possible approaches, pixellating the mass makes it is easy to enforce non-negativity of the mass distribution.
- Pixellate $\kappa(\boldsymbol{\theta})$ and use maximum entropy. See Bridle et al. (this volume) for an example of this in a somewhat different context.

The regularization we applied is to minimize

$$\int \left(\kappa - \frac{\langle \kappa \rangle}{\langle L \rangle} L \right)^2 d^2\boldsymbol{\theta} + \epsilon^4 \int (\nabla^2 \kappa)^2 d^2\boldsymbol{\theta} \quad (10)$$

while of course enforcing all the lensing constraints. The first term in (10) tends to minimize mass-to-light variation, since $\langle \kappa \rangle / \langle L \rangle$ is a mean M/L . The second term tends to smooth, with ϵ a sort of smoothing scale. By regularizing with respect to different light distributions we can get an estimate of the uncertainty.

Since the regularizing functional (10) is quadratic in κ , minimizing it subject to the linear lensing constraints is readily implemented through quadratic

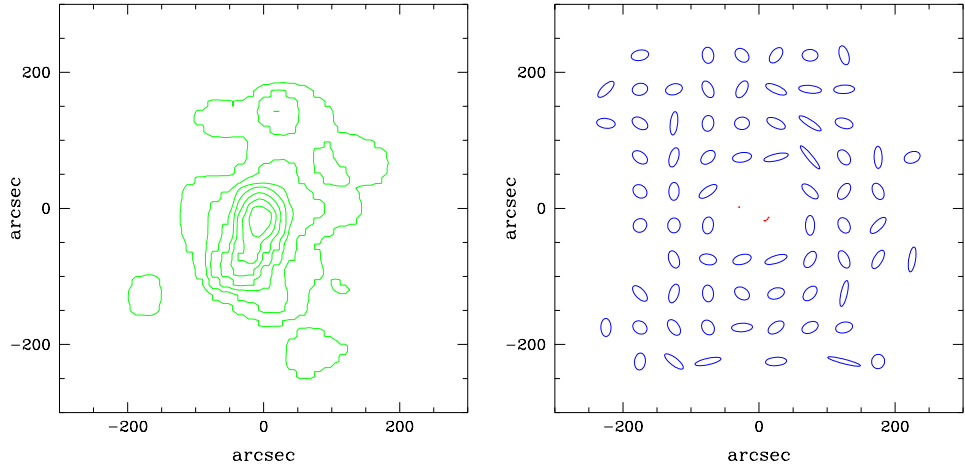


Figure 3. **Left:** Cluster luminosity contours in Cl1358+62. from the catalog of galaxy V_z 's in van Dokkum et al (1998). Likened at the conference to a left facing seahorse with a ponytail. **Right:** Shear map (exaggerated by a factor of 5) from Hoekstra et al (1998). We have excised the central region to avoid averaging the shear where it is varying rapidly. Also note that unlike Fig. 14 in Hoekstra et al., we have binned without smoothing here.

programming algorithms. The disadvantage is that the storage needed is $\simeq 2 \langle \text{number of pixels} \rangle^2$ limiting us to of order 5000 pixels. The solution is to have adaptive pixellation (much like tree codes in N -body simulations), with smaller pixels for the inner parts of the cluster and large pixels outside.

4. The mass-sheet degeneracy

After enthusing about how easy lens reconstruction is, it is well to make a cautionary remark about the main source of uncertainty. Here again, the arrival-time surface is very useful.

If we multiply $\tau(\boldsymbol{\theta})$ by a constant factor, we just stretch the surface vertically, and geometrically it is clear that neither image locations nor their relative magnifications change. More formally, we can rearrange Eq. (2) and drop the irrelevant term $\frac{1}{2}\boldsymbol{\beta}^2$ to get

$$\tau(\boldsymbol{\theta}) = 2\nabla^{-2} \left(1 - \frac{D_{\text{ls}}}{D_s} \kappa \right) - \frac{1}{2} \boldsymbol{\theta} \cdot \boldsymbol{\beta}. \quad (11)$$

If we now multiply both $(1 - D_{\text{ls}}/D_s \kappa)$ and $\boldsymbol{\beta}$ by some constant a , the image structure will be unchanged; only time delays and total magnification will get multiplied by a and a^{-1} respectively (the latter because rescaling $\boldsymbol{\beta}$ rescales all the sources). Therefore lens reconstruction from image structure (without absolute magnifications) leaves $(1 - D_{\text{ls}}/D_s \kappa)$ uncertain by a constant factor. This is the mass-sheet degeneracy.

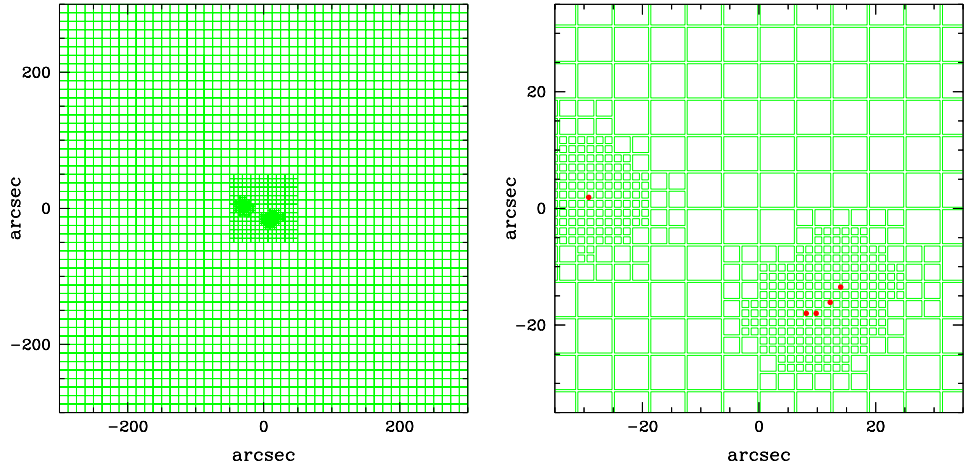


Figure 4. Pixellation used for the mass reconstruction of the Seahorse cluster. Note that it is completely adaptive, and allows us to increase the resolution at any desired place—in this case the region around the red arc. **Left:** The full field. **Right:** The inner region, with dots marking features in the red arc.

It may appear at first that the mass-sheet degeneracy can be eliminated by requiring κ to vanish at large distances. But outside the observed region, the monopole part of κ is completely unconstrained. So the mass-sheet degeneracy is equally effective with a mass disk larger than the observed region. Figure 2 illustrates.

5. Reconstruction of Cl 1358+62 (The Seahorse Cluster)

This cluster seemed the obvious test case for combined strong and weak lensing reconstruction in a relatively large field. The cluster itself is at $z = 0.33$ and its inner part lenses a $z = 4.92$ galaxy into a red arc; this was identified by Franx et al. (1997) who also presented a strong lens model. Hoekstra et al. (1998) measured the shear field in an HST WFPC2 mosaic and reconstructed a mass map from weak lensing. The present work combines both regimes.

Figure 3 illustrates the data on this cluster that we have used: a shear field derived by binning the individual polarization measurements kindly provided by Hoekstra and collaborators and assuming a constant $z = 1$ for the background galaxies, and a smoothed V_z light distribution. Figure 4 shows the pixellation we used.

Figure 5 is our mass map, computed by regularizing with respect to the light and a smoothing scale ϵ changing from $\simeq 5''$ in the center to $\simeq 1'$ at the edge. Our estimated uncertainty is derived from an ensemble of reconstructions where we rotated the light map by arbitrary angles and shifted it randomly by up to $100''$ and regularized with respect to these altered light maps. The mass map resembles Fig. 15 of Hoekstra et al. (1998) but tends to be smoother. Also the overall normalization is somewhat higher; this is probably due to different

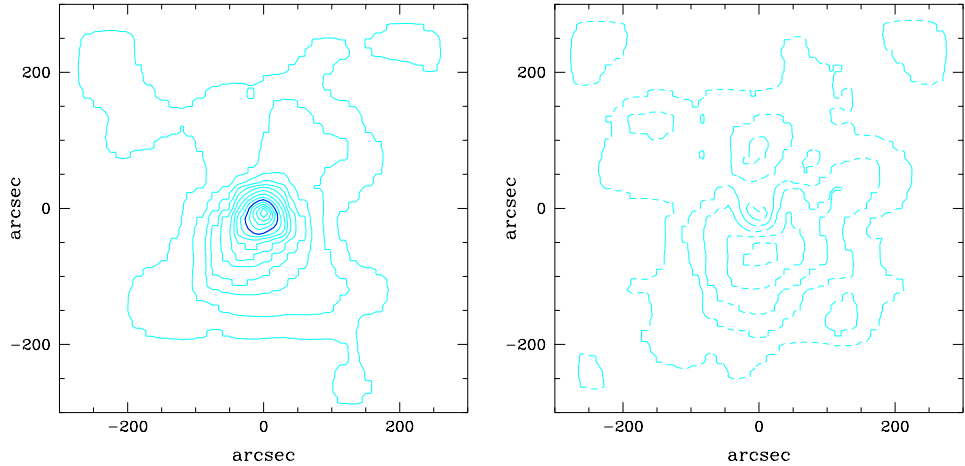


Figure 5. Mass map of the Seahorse cluster. **Left:** Contours of κ in steps of 0.1. **Right:** Contours of $\Delta\kappa$ in steps of 0.025.

treatments of the boundary, though with the mass-sheet degeneracy. (The red arc at $z = 4.92$ compared to $z = 1$ assumed for the weakly lensed galaxies, reduces the effect of the mass-sheet degeneracy, but does not eliminate it.) Our central density is higher, but this is as expected since inclusion of a multiply-imaged system immediately forces $\kappa > 1$. There is some indication that the mass peak is offset (by some 10s of kpc) to the south of the light peak, a natural thing to expect if the cluster is asymmetric and galaxy formation is biased. But this offset is tentative; in Abell 2218, where the inner region is much richer in lensing and better constrained, the evidence for an offset is more compelling (AbdelSalam et al. 1998).

Figure 6 shows the enclosed mass out to different radii and the reconstructed shear. It is surprising that the enclosed mass after angular averaging, looks so ‘isothermal’ even though the mass map is very asymmetric. We obtain $M = (10 \pm 1) \times 10^{14} M_{\odot} \text{Mpc}^{-1}$, corresponding to a formal Einstein radius of $43''$ and a formal isothermal los dispersion of $(990 \pm 70) \text{km sec}^{-1}$. The estimated mass-to-light is $(380 \pm 60) h M_{\odot} L_{\odot V}^{-1}$. The CNOC survey (Carlberg et al. 1997) measured 910km sec^{-1} for the los velocity dispersion and estimated $M/L = 229 h^{-1} M_{\odot} L_{\odot V}^{-1}$.

6. Discussion

We have developed a mass reconstruction technique that deals with all the cluster lensing regimes simultaneously, from multiple images in the central regions to weak shear in the outer regions, and moreover with adaptive resolution. Code implementing this is available from the authors. Variants of our technique (suggested in Section 3) may also be of interest in future work.

At this stage it appears that cluster mass reconstruction is very good at recovering *features*—a good example are offsets between mass and light peaks

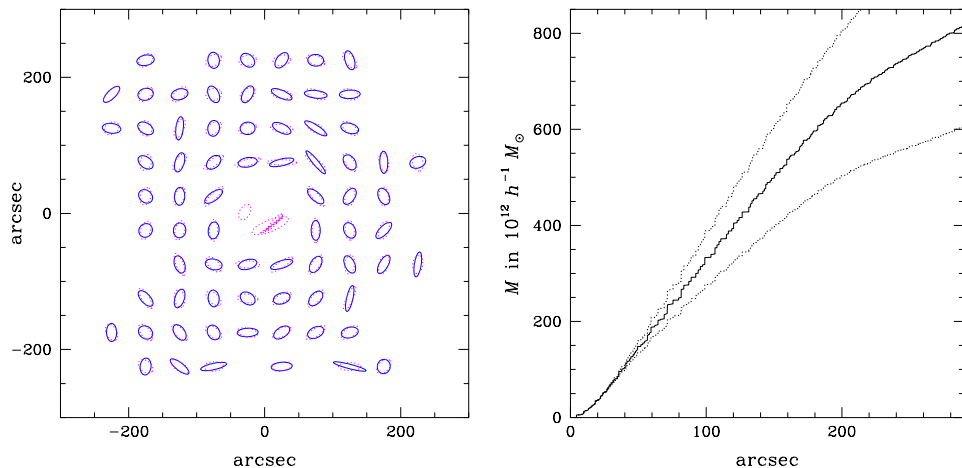


Figure 6. **Left:** Shear map. The superimposed ellipses show the observed and reconstructed (dotted) shear, both exaggerated by a factor of five. As we might expect, the reconstructed shear appears more correlated than the observed. The ellipses in the inner region show the reconstructed shear (not exaggerated) at the locations of the red arc. **Right:** Enclosed mass and estimated uncertainty.

in clusters, which may be indirect evidence for biased galaxy formation. But the *calibration* of the mass (even with perfect shear data) is still problematic—the mass sheet degeneracy is a vicious effect. We suggest that recovering the redshift distribution and the absolute magnification of the background galaxies (even with large uncertainties) are the best hope of breaking this degeneracy, and is likely to be very rewarding in future work.

Acknowledgments. We are grateful to Henk Hoekstra and collaborators for supplying us with their shear data on Cl 1358+62.

References

- AbdelSalam, H.M., Saha, P., & Williams, L.L.R. 1998, AJ, 116, 1541
 Bridle, S.L., Hobson, M.P., Lasenby, A.N., Saunders, R., this volume
 Carlberg, R.G., Yee, H.K.C., Ellingson, E. 1997, ApJ, 478, 462
 van Dokkum, P.G., Franx, M., Kelson, D.D., Illingworth, G.D., Fisher, D., Fabricant, D. 1998, ApJ, 500, 714
 Dye, S., & Taylor, A. 1998, MNRAS, 300, L23
 Franx, M., Illingworth, G.D., Kelson, D.D., van Dokkum, P.G., Tran, K.-V. 1997, ApJ, 486, L75
 Hoekstra, H., Franx, M. Kuijken, K., Squires, G. 1998 ApJ, 504, 636